

Optimisation and management of energy generated by a multifunctional MFC-integrated composite chassis for rail vehicles

Item Type	Article
Authors	Liu, Yiding;Du, Sijun;Micallef, Christopher;Jia, Yu;Shi, Yu;Hughes, Darren
Citation	Liu, Y., Du, S., Micallef, C., Jia, Y., Shi, Y., & Hughes, D. J. (2020). Optimisation and management of energy generated by a multifunctional MFC-integrated composite chassis for rail vehicles. <i>Energies</i> , 13(11), 2720. https://doi.org/10.3390/en13112720
DOI	10.3390/en13112720
Publisher	MDPI
Journal	Energies
Download date	2026-05-19 16:18:18
Item License	https://creativecommons.org/licenses/by/4.0/
Link to Item	http://hdl.handle.net/10034/623463

1 Article

2 Optimisation and management of energy generated 3 by a multifunctional MFC-integrated composite 4 chassis for rail vehicles

5 Yiding Liu ¹, Sijun Du ², Christopher Micallef ¹, Yu Jia ^{3,4,*}, Yu Shi ^{4,*}, and Darren J. Hughes ^{1,*}

6 ¹ Warwick Manufacturing Group, University of Warwick, Coventry CV4 7AL, UK;
7 Yiding.liu@warwick.ac.uk (Y.L.); Christopher.Micallef@warwick.ac.uk (C.M.)

8 ² Department of Electrical Engineering and Computer Sciences, University of California at Berkeley,
9 Berkeley CA 94720, USA; sijun@berkeley.edu (S.D.)

10 ³ School of Engineering and Applied Science, Aston University, Birmingham B4 7ET, UK;

11 ⁴ Department of Mechanical Engineering, University of Chester, Chester CH2 4NU, UK;

12 * Correspondence: yu.jia.gb@ieee.org (Y.J.); y.shi@chester.ac.uk (Y.S.); D.hughes@warwick.ac.uk (D.H.)

13 Received: date; Accepted: date; Published: date

14 **Abstract:** With the advancing trend towards lighter and faster rail transport, there is an increasing
15 interest to integrate composite and advanced multifunctional materials in order to infuse smart
16 sensing and monitoring, energy harvesting and wireless capabilities within the otherwise purely
17 mechanical rail structures and the infrastructure. This paper presents a holistic multiphysics
18 numerical study, across both mechanical and electrical domains, that describes an innovative
19 technique of harvesting energy from a piezoelectric micro fibre composites (MFC) built-in
20 composite rail chassis structure. Representative environmental vibration data measured from a rail
21 cabin has been critically leveraged here to help predict the actual vibratory and power output
22 behaviour under service. Time domain mean stress distribution data from the Finite Element
23 simulation was used to predict the raw AC voltage output of the MFCs. Conditioned power output
24 was then calculated using circuit simulation of several state-of-the-art power conditioning circuits.
25 A peak instantaneous rectified power of 181.9 mW was obtained when an eight-stage Synchronised
26 Switch Harvesting Capacitors (SSHC) from eight embedded MFCs located. The results showed that
27 the harvested energy could be sufficient to sustain a self-powered structural health monitoring
28 system with wireless communication capabilities. This study serves as a theoretical foundation of
29 scavenging of vibrational power from the ambient state in a rail environment as well as to pointing
30 to design principles to develop regenerative and power neutral smart vehicles.

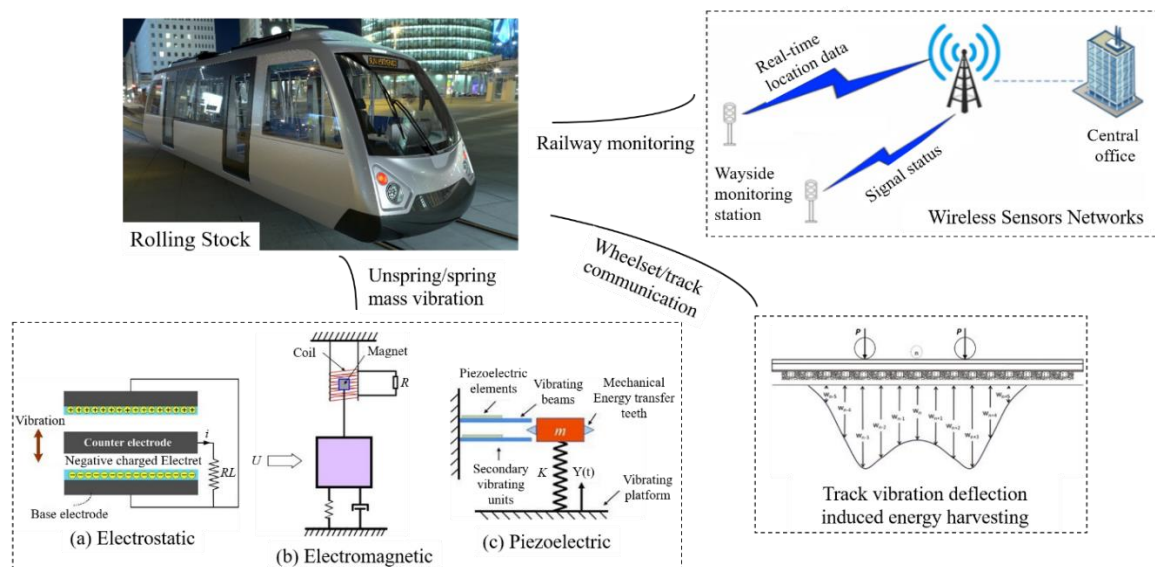
31 **Keywords:** vibration energy harvesting; micro fibre composite; finite element analysis; circuit
32 design and optimization; power conditioning circuit; lightweight rail vehicle
33

34 1. Introduction

35 Rail transport, as a means of transit for passengers and goods in daily life, is now increasingly
36 targeting and transforming towards lightweight, faster speeds and net zero carbon emissions. The
37 current state-of-the-art in the automotive sector suggests to use “right material in the right place” to
38 satisfy the stiffness, strength and crashworthiness certification requirements. This leads to the
39 application of composite materials, such as carbon fibre or glass fibre reinforced polymers due to
40 their lighter weight and high stiffness-to-weight ratio. Subsequently, particularly in light of the global
41 energy crisis and environment concerns, smart composites with energy harvesting capabilities have
42 developed into an attractive research frontier [1]. Vibrations exists throughout the rail transportation
43 system, such as the vibration of floor and vehicle chassis, railway train or tracks, etc. and hence it
44 could offer an alternative energy source to compensate for the dissipation of kinetic energy during

45 vehicle vibration and motion [2].

46 Vibration-based energy harvesting, as one of the most promising research fields, has been
 47 established utilising electromagnetic generators [3], piezoelectric generators [4,5], MEMS-scale
 48 electrostatic generators [6], triboelectric [7,8] and magnetostrictive effects [9]. Figure 1 illustrates the
 49 means of energy harvesting mechanisms and their application possibilities to the railway industry,
 50 adopted from [10–15]. However, the application of different energy harvesting systems depends on
 51 the specific requirements, i.e. environmental conditions and physical constraints [16].
 52 Electromagnetic inductions produce energy harvesting by means of permanent magnets, a coil and a
 53 resonating cantilever beam, however, magnets also add to the inertial mass [17]. Electrostatic
 54 generators require an initial constant polarisation of voltage field or charge. When using electrets to
 55 provide the initial charge, the output impedance is often quite high which makes them less suitable
 56 as a power supply [17]. Among them, piezoelectric materials offer great benefit to convert mechanical
 57 energy into electric energy due to their relatively high energy density and scalability [16,18]. As
 58 conventional piezoelectric ceramics are brittle and easily broken, the macro-fibre composite (MFC)
 59 can be used as energy harvesting device due to its structural flexibility, high efficiency and almost
 60 negligible thickness, which has been successfully developed by Shi's work investigating their
 61 application into an aircraft's wing structure [19] and Yuan's work on a one tenth scale experimental
 62 rig of a urban rail vehicle [20].



63 **Figure 1.** Illustration of energy harvesting applied to the railway industry, adopted from [10–15].

64 With respect to energy harvesting specific for railway application, most studies have focused on
 65 the vehicle brakes, shock absorbers, and exhaust systems and rail/track interfaces. Numerous
 66 research endeavours have been extended to investigate the energy harvesting potential from railway
 67 tracks as the tracks sustains the full load of the vehicle when the train moves [1]. Zuo et al. [1] stated
 68 that the actual harvested power from railway tracks depends on the speed of the train, the weight of
 69 the train and the type of railway track. For instance, for a four-wheel railcar of 100 tonnes at a speed
 70 of 40 miles/h, the average power potential is about 2 kW under 6.35 mm track deflection according
 71 to analytical analysis. This amount of power is sufficient for most of the trackside electric facilities,
 72 e.g. typically the light-emitting diode (LED) signal lights require a power of 8–10 W and level-crossing
 73 gates requires a power of 150–200 W [1]. Pourghodrat et al. [21] proposed a hydraulic energy
 74 harvesting system to harness power from both downward and upward deflections of the track. The
 75 system could provide an average power of 1.9 W under a deflection of 2.8 mm and maximum load
 76 of 6.4 t. Hadas et al [22] developed a model-based design of various harvesting systems embedded
 77 inside track sleepers and the maximum predicted harvested power was around 2 W during train
 78 passing at speed.

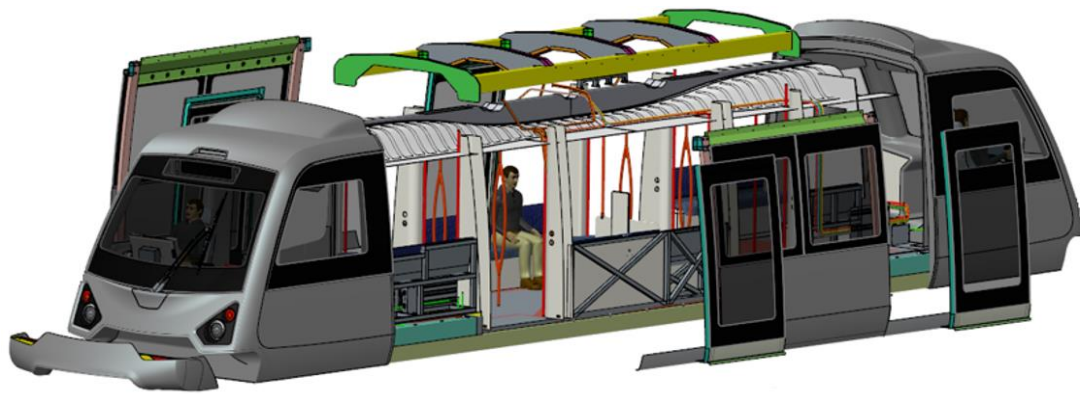
79 The works above discussed comparably in large-scale energy harvesting at 1 W to 100 kW which

80 promised a solution for self-powering the active devices, such as energy recovery from a suspension
81 [2]. However, a fundamental challenge is that such large-scale vibrations are rarely maintained at
82 time-varying frequency and at alternating velocities, resulting in the energy harvested unsustainable,
83 inefficient and eventually unreliable for powering functional devices. However, small-scale
84 vibrations are too difficult to avoid during service of rail vehicles and ideally meeting the energy
85 request under sustainable supplying if they could be efficiently harvested. Hence, the balance of
86 combined vibration control and efficiency of energy harvesting could be a critical concern considered
87 for small-scale vibration harvesting. So far, the most micro-scale harvested power ranging from
88 10 μ W to 100 mW was significantly ignored in the railway industry, especially the vibrations from
89 the vehicle structures when running on the individual routes and therefore wasted. However, such
90 energy could be the important source for self-powering the wireless sensors and low-power
91 electronics, which effectively resolves the difficulties of connections by wires/cables during assembly
92 and induced extra weight. The current study is focusing on these micro-scale powers harvested from
93 the composite chassis of rail vehicle under a low frequency operational vibration. Considering the
94 power requirement of sensing and wireless sensor nodes for communication [23], the optimisation
95 and energy management during harvesting process is numerically predicted for the real-world
96 implementations of rail sectors based on our previous works presented in [24] and [25].

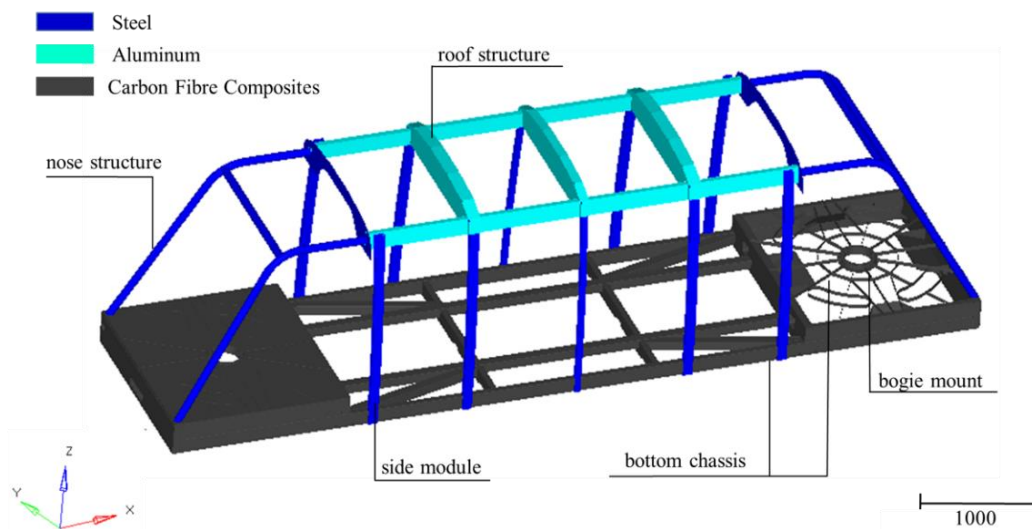
97 Most existing piezoelectric models are either based on analytical analysis (based on beam theory)
98 [16,26–28] or experimental tests [20–22]. Analytical models are beneficial in understanding the
99 underlying physics, however, it is difficult to simplify the complicated geometries. Experimental
100 evaluations are useful to provide situations that are more realistic, however, they are time and cost
101 consuming and the results are highly subjective due to the possibility of human error. On the other
102 hand, finite element (FE) models can support complex assemblies while including multi-physical
103 modules. Jia and Shi et al. [28] proposed using an FE model to simulate the electrical and mechanical
104 behaviour of an integrated MFC on a carbon fibre composite beam using COMSOL Multiphysics
105 combining solid mechanics, electrostatic and electrical-circuit-physics models. It has specific
106 requirement on the computer hardware if applied to a large complex geometry including multi
107 modules.

108 This work specifically relates to an industrial challenged project at Warwick Manufacturing
109 Group (WMG), the University of Warwick, where a new class of lightweight rail vehicle is in
110 development for upgrading the transportation system of the City of Coventry and lowering the
111 carbon emissions [29]. The vehicle under development follows a “right material in the right place”
112 strategy adopted from the design of automotive vehicle. Figure 2(a) shows an exploded view of the
113 main components design of the rail vehicle. The prototype design includes a steel bottom chassis and
114 side module, an aluminium roof structure and composite nose mould to improve the stiffness of the
115 vehicle from the safety perspective. However, in order to further reduce the weight to improve the
116 driving performance and efficiency, the composite bottom chassis was proposed with an expect of
117 weight saving of 33.5% (from 922.3 kg to 613.5 kg). Moreover, through the optimisation of the
118 efficiency of energy harvesting, composite bottom chassis is also ideal due to a higher stress
119 distributed with integration of piezoelectric energy harvesters.

120 This paper aimed at harvesting energy from a multifunctional MFC-embedded composite
121 chassis of a simplified rail vehicle structure (Figure 2(b)), under the representative operational
122 vibration data measured in a rail cabin. The design of the pattern and location of the integrated MFCs
123 within composite chassis was determined by a parametric finite element (FE) study. To meet the
124 actual power demanding of sensors and wireless nodes, the harvested energy was optimised and
125 managed by designing the various rectified circuits strategies. The recoverable rectified power from
126 the chassis vibration was predicted with optimal energy saved compared to other rectification circuit
127 designs. The feasibility of using the harvested energy to sustainably power the smart microsystems
128 was assessed by referring to the power consumptions of such functional components. Figure 3
129 summarise the schematic of the FE model setup and the power prediction system discussed in this
130 paper.



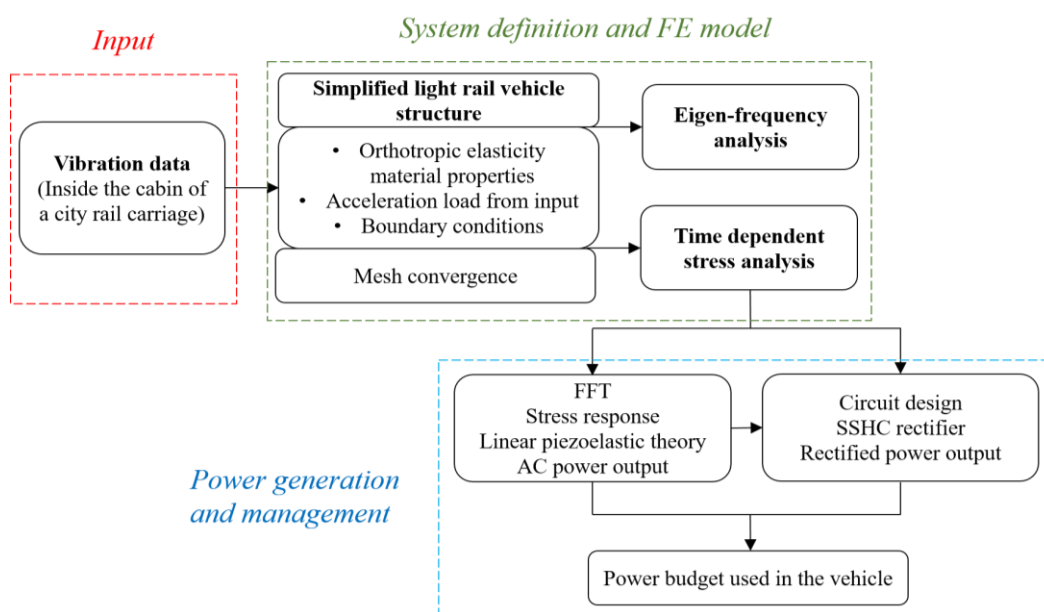
(a) Exploded view of the main components in the vehicle



(b) Simplified vehicle structure studied in this paper

132
133
134

Figure 2. (a) Exploded view of the main components in the rail vehicle; (b) multi-material design of a simplified light rail vehicle structure. Units in mm. The vehicle length, width and height are 11.0, 2.7 and 3.1 m, respectively.



135
136
137

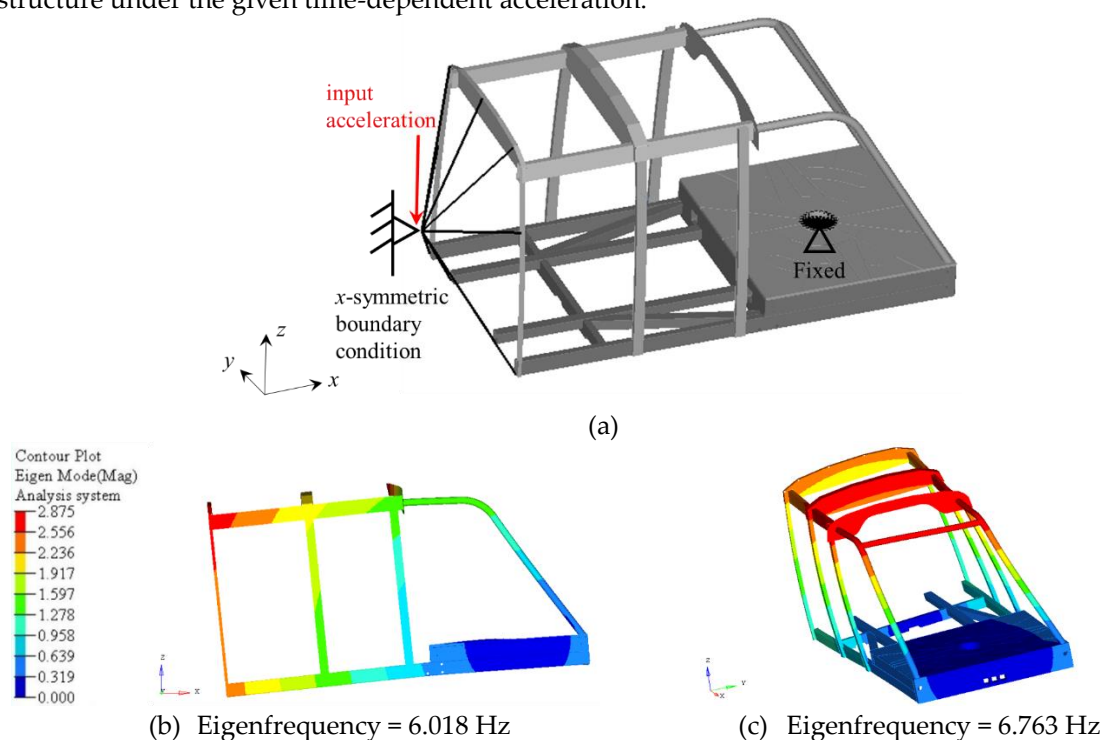
Figure 3. The schematic of the FE model setup and power prediction from the piezoelectric MFC on composite rail chassis when subjected to vibrational data input discussed in this paper.

138 2. Finite element analysis of the vehicle

139 2.1. Finite element modal

140 For balancing the computing efficiency with a full chassis structure, the symmetric model of the
 141 vehicle structure was created using Hypermesh code and OptiStruct solver. A shell model was built
 142 by extracting the middle surface from the three-dimensional geometry to save computational cost
 143 and time. A global element size of 10 mm was confirmed after a parametric study of convergence in
 144 the FE solver. The entire chassis structure was primarily joined by rigid connections between different
 145 structural components. The definition of boundary conditions of the chassis is illustrated in Figure
 146 4(a): the displacement and rotations of the bogie mount central was restricted as the bogie structures
 147 are attached to the wheel and stay stable on the track. Multi-point constraint was used to link all the
 148 nodes at the middle section to a built independent node and an x -symmetric boundary condition was
 149 employed. The time-dependent accelerations were input to the built independent node and the
 150 deformations were expected to be transferred to the entire chassis.

151 The steel and aluminium structural components were modelled using isotropic natures, with
 152 the material properties shown in Table 1. The composite bottom chassis was made from RC200T
 153 woven fabric CFRP, with the orthotropic material properties obtained from [28] (also shown in Table
 154 1). An Eigenfrequency study of the half chassis structure was firstly performed and the analysis
 155 revealed the natural frequency at 6.018 Hz (1st bending mode, see Figure 4(b)) and 6.763 Hz (1st
 156 torsional mode, see Figure 4(c)), with higher resonant modes summarised in Table 2. Time dependent
 157 transient response analysis was carried out to determine time-varying dynamic responses of the
 158 structure under the given time-dependent acceleration.



159 **Figure 4.** (a) Boundary conditions of the FE model of the vehicle, (b) 1st bending mode (6.018 Hz) and
 160 (c) 1st torsional mode (6.763 Hz) of the vehicle.

161 **Table 1.** Properties of the materials used in the vehicle structure
 162 (material breakdown in Figure 2(b)).

	Elastic modulus (GPa)	Poisson's ratio	Density (kg/m ³)
Steel	210	0.29	7850
Aluminium	69	0.3	2700

CFRP (RC200T) [28]	$E_x = 59.45, E_y = 60.30, E_z = 3.90$ $G_{xy} = 62.90, G_{yz} = 1.50, G_{xz} = 62.35$	$\nu_{xy} = 0.3$ $\nu_{yz} = 0.4$ $\nu_{xz} = 0.3$	1800
--------------------------	---	--	------

163

Table 2. Comparison of resonant frequencies for various modes of the vehicle.

Mode	Freq. (Hz)
1 st bending (Figure 4(b))	6.018
2 nd bending	19.935
1 st torsional (Figure 4(c))	6.763
2 nd torsional	14.407
3 rd torsional	21.921
1 st lateral	23.839

164

2.2. *Vibration data analysis*

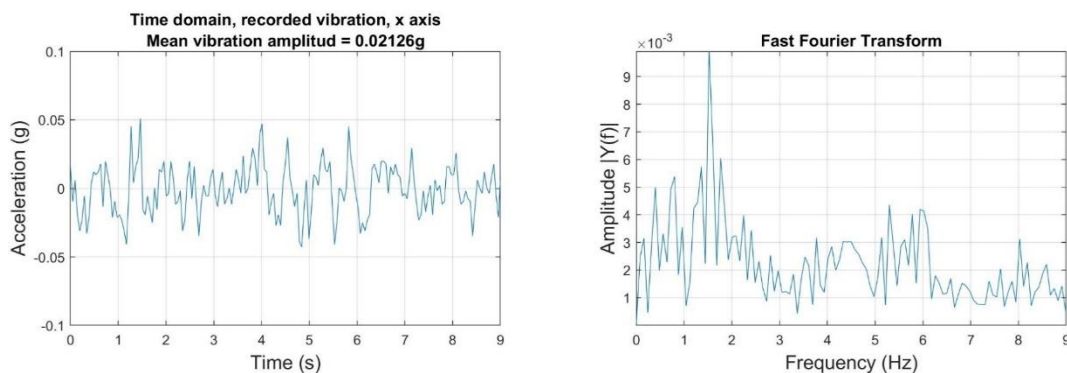
165

Vibration data was measured directly from a representative environment inside the cabin of a city rail carriage using 3 axis Gulf Coast Data Concepts (GCDC) MEMS accelerometer data loggers with a sample rate of 400 Hz to 800 Hz [30] and has been published in [28]. The total period of the selected data covers approximately 9 s. The axes were defined identical to the coordinate shown in Figure 4(a): x-axis is along the vehicle, y-axis is across the vehicle, and z-axis is vertical through the vehicle. The time domain data were processed and analysed using Fast Fourier Transform (FFT) in MATLAB, as shown in Figure 5. X-axis vibration (mean amplitude was 0.02126 g) contained an evident frequency peak at 1.53 Hz, followed by harmonics at approximately 6 Hz. Y-axis (mean amplitude was 0.01205 g) was more broadband, with a few harmonics at different frequencies. Z-axis vibration (mean amplitude was 0.03007 g) experienced peaks at 1.28 Hz, with a flat active frequency range covering up to 10 Hz. All of the accelerations from the three axes contribute to the movement of the vehicle. It should be noted that the vibration data in the three axes depends on many factors, i.e., the health condition of the vehicle, the track roughness. These acceleration data were used as excitation inputs for the FE model.

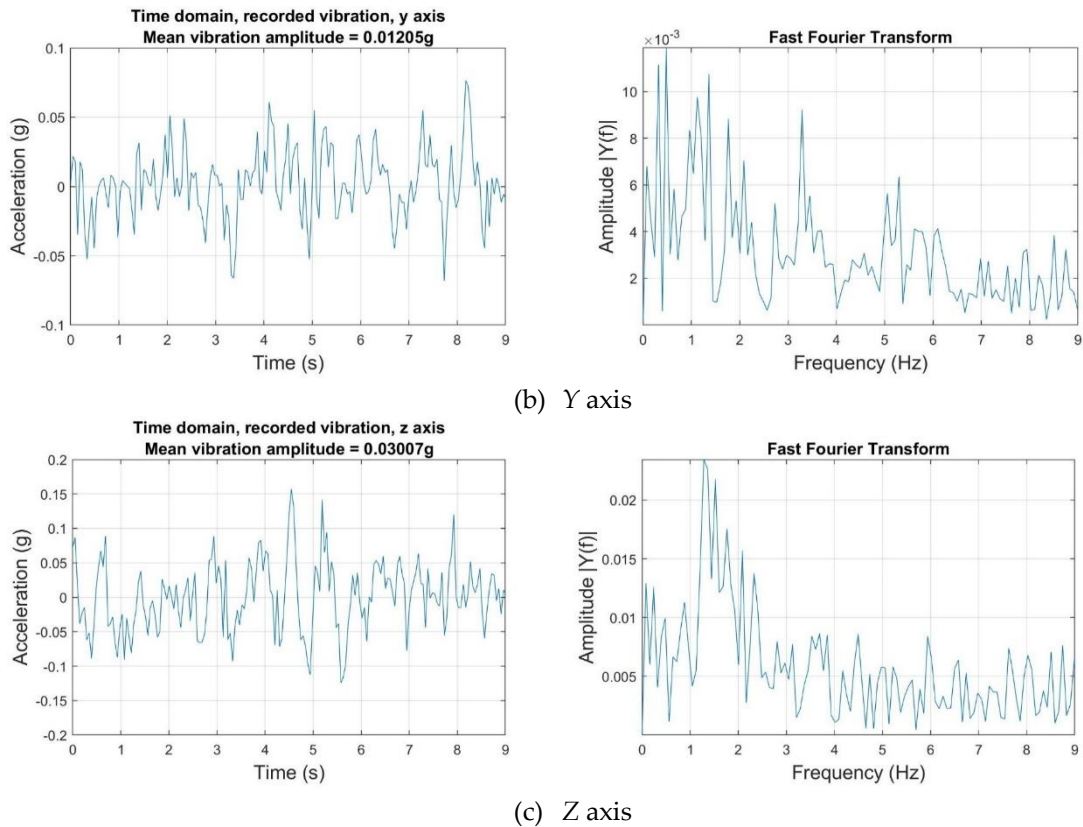
171

It should be noted that the natural frequency of the prototype structure at 6.018 Hz does not match with the first active frequency peak of the three axes vibration data, therefore, the power response was primarily non-resonant for the unmatched case.

172



(a) X axis



(b) Y axis

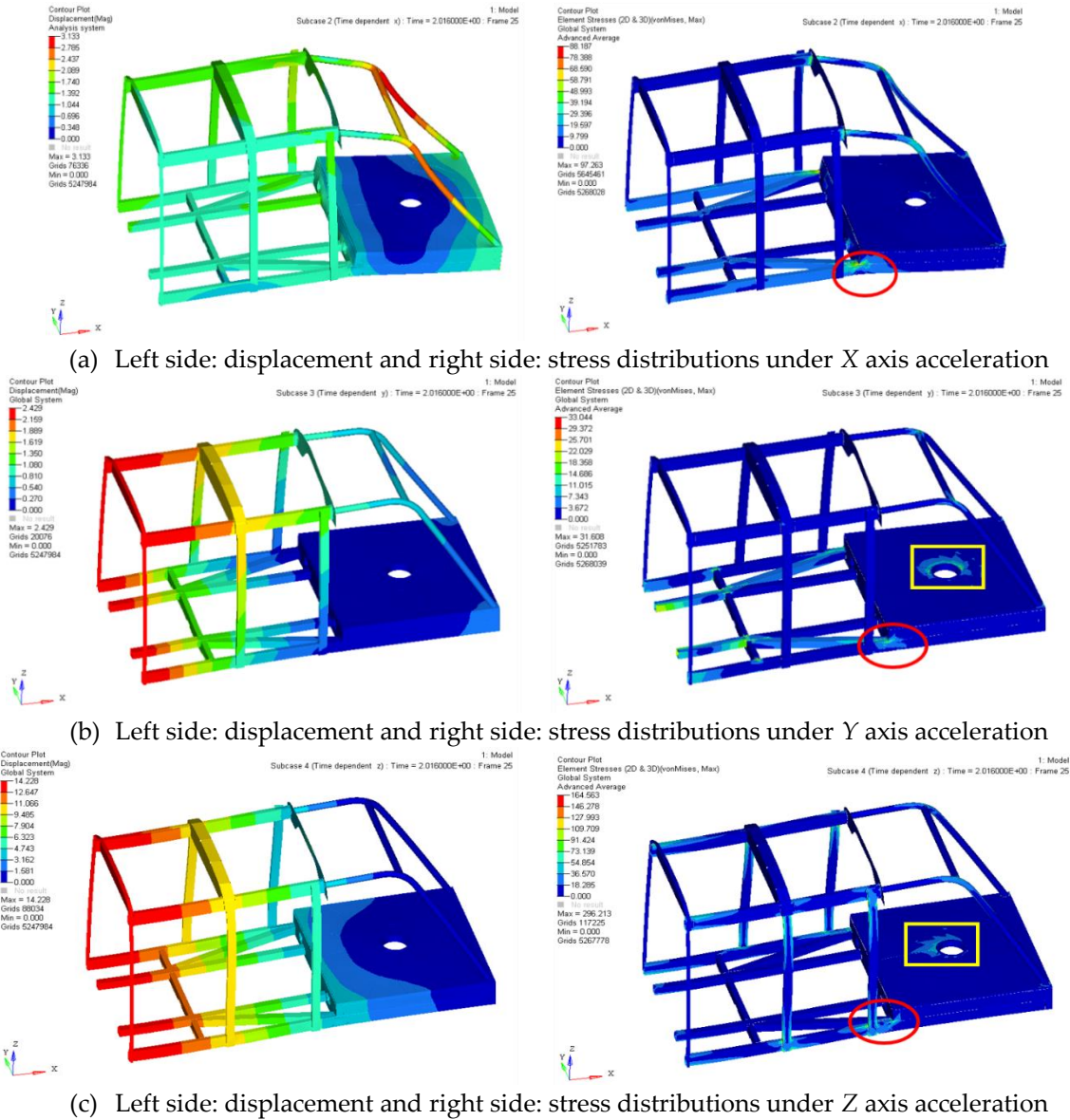
(c) Z axis

183 **Figure 5.** Representative environment vibrations for three axes of train cabin interior, including time
 184 domain vibration data and FFT analysis.

185 2.3. Stress responses used for power prediction

186 The aim at obtaining the stress responses in this section is used as input for power prediction.
 187 Apparently, the stresses on the half chassis structure varies with the time-dependent accelerations.
 188 For example, the displacements and von Mises stress responses under three axes accelerations at
 189 randomly selected 2.016 s are shown in Figure 6. The chassis behaves in lateral and bending mode
 190 under Y and Z-axis accelerations, respectively, with a maximum displacement of 2.43 mm and
 191 14.23 mm at the middle of the chassis. Under X-axis acceleration, the chassis structure performs in
 192 primarily longitudinal bending deformation, with the nose structure deforming a maximum of
 193 3.13 mm. Considering at the stress distributions under three axes, stress concentrates at the lower
 194 chassis connection points (red circle in Figure 6) and around the bogie mount central (yellow box in
 195 Figure 6). A larger stress can also be observed on the chassis beams when Z-axis acceleration is
 196 employed due to the bending deformation.

197 Figure 7 indicates the relationship of von Mises stress vs. time of two elements located at the
 198 highest stressed lower chassis and bogie mount central. The signs of the stresses are defined in
 199 alignment with the directions of the displacements according to the local axes. The stresses at the two
 200 locations peak at approximately 100 MPa, respectively at around 8.5 s and 3.5 s, which is much
 201 smaller than the tensile strength of the composite materials (662 MPa [31]). It can be seen that the
 202 vibration at the bogie mount fluctuates more than that at the lower chassis indicating a less stable
 203 design.



204
205
206
207

Figure 6. Left side: displacement and right side: stress distributions of the half chassis model under (a) X-axis (Scale factor=100), (b) Y-axis (Scale factor=100) and (c) Z-axis (Scale factor=50) accelerations at 2.016 s; red and yellow box circles the high stress regions at lower chassis connection and bogie mount, respectively.

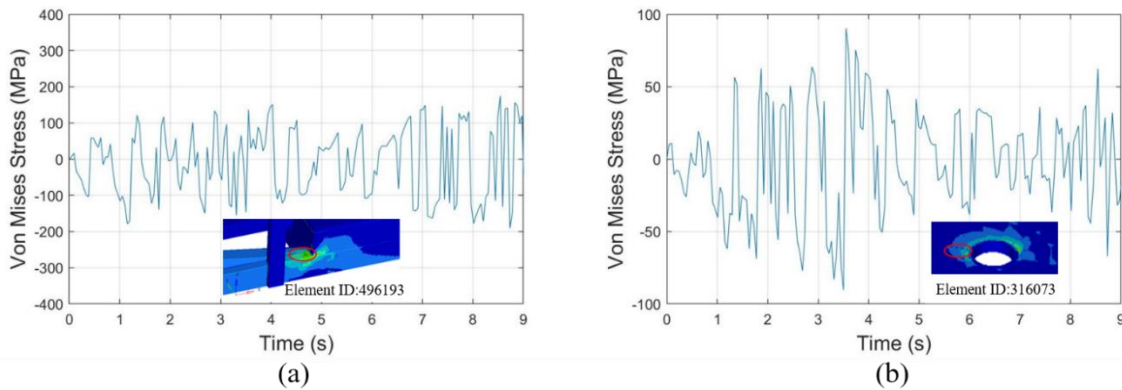


Figure 7. Von Mises stresses vs. time plots of (a) lower chassis connecton, and (b) bogie mount central.

208 3. Power generation and Management

209 3.1. AC power prediction using MFC piezoelectric material

210 The embedded MFC-P2 transducers with designed shape of geometry and dimensions from [32]
 211 can be used as the energy harvester. The MFCs were modelled as orthotropic materials using the
 212 mechanical properties presented in Table 3, with E_1 and E_2 aligned to the rod and electrode
 213 directions, respectively. The piezoelectric and dielectric properties of the MFC are shown in Table 4.
 214 In accordance with the time-varying stress distributions in the chassis structure obtained from FE
 215 analysis considering the aim to harvest highest power, eight MFC location possibilities (as shown in
 216 Figure 8(b)) were evaluated which cover the stress concentration areas and high stress regions. MFC 1
 217 to MFC 4 are designed in rectangular geometry of $100 \times 50 \times 0.3 \text{ mm}^3$ and MFC 5 (same as MFC 6) to
 218 MFC 7 (same as MFC 8) are designed in triangular shape with an area domain of 13488.2 mm^3 and
 219 17789.3 mm^3 to fit the geometry of the bogie mount structures.

220 **Table 3.** Mechanical properties of MFC [32], E_x and E_y are elastic modulus in the rod and electrode
 221 directions, respectively.

E_x (GPa)	E_y (GPa)	G_{xy} (GPa)	ν_{xy}	Density (kg/m^3)
30.34	15.86	5.52	0.31	5400

222 **Table 4.** Piezoelectric and dielectric properties of MFC [32].

Charge constant d_{31} (pC/N)	-170
Charge constant d_{33} (pC/N)	400
Capacitance per unit area C_p (nF/cm ²)	7.8
Dielectric permittivity ϵ_p	0.15

223

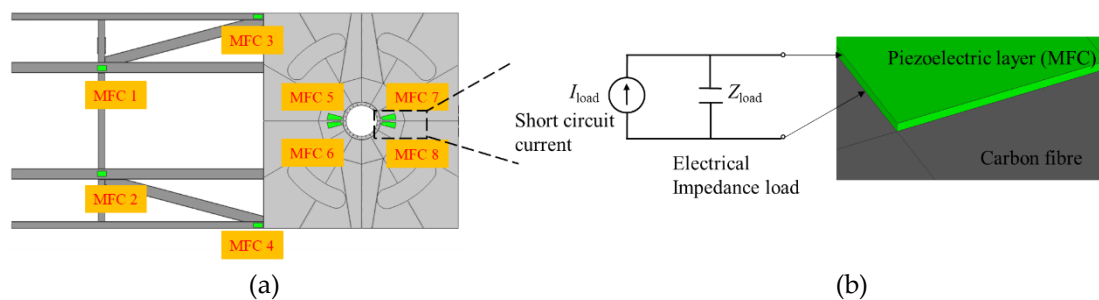


Figure 8. (a) The location possibilities of the MFC transducers on carbon fiber chassis structure, (b) the magnitude of the MFC transducer used to generate electrical power based on an electrical load, Z_{load} .

224 The time-varying stress responses from the MFC piezoelectric materials was calculated from the
 225 time dependent analysis of the global vehicle FE model. Typically, the MFC used in the chassis is
 226 ideally suited for vibration energy harvesting even in higher modes, as the opposing stress regions
 227 across the single MFC element which might result in partial charge cancellation has not been
 228 observed from the FE simulation. This is because the deformation in the MFC region is comparatively
 229 small and consistent compared to the large deformation of the entire vehicle. When used as energy
 230 harvester, the piezoelectric material can work in d_{31} or d_{33} mode depending on the poling direction
 231 and the stress direction. It is typical that the d_{31} mode is usually seen in piezoelectric films, where the
 232 electric field is perpendicular to the direction of mechanical strain; d_{33} mode appears as piezoelectric
 233 stacks where both electric field and strain are in the poling direction. As charge constant, d , is defined
 234 as the short circuit charge density per applied mechanical stress, the generated short circuit charge
 235 and current can be summarised by equations (1) and (2) [28],

$$Q_{sc}(t) = d_{31} \sigma_{av}(t) \int_A dA \quad (1)$$

$$I_{sc}(t) = \omega(t) d_{31} \sigma_{av}(t) \int_A dA \quad (2)$$

236 where Q_{sc} is the short circuit electrical charge; I_{sc} is the short circuit current; σ_{av} is the average
 237 stress experienced by the piezoelectric domain and A is the active area of the piezoelectric domain; ω
 238 is the frequency where the piezoelectric transducer excites, FFT was carried out on the time domain
 239 response from the FE simulation in order to assess the frequency characteristics.

240 For a given electrical impedance load Z_{load} , the current generated across the load, $I_{load}(t)$ is given
 241 by equation (3). To maximise power output, the impedance matching is needed between Z_{load} and Z_i .

242 For short circuit, $Z_{load} = 0$, the factor $\frac{Z_i}{\sqrt{Z_i^2 + Z_{load}^2}} = 1$. As $Z_{load} \rightarrow \infty$, $\frac{Z_i}{\sqrt{Z_i^2 + Z_{load}^2}} \rightarrow 0$. Therefore the

243 generated power across a matched impedance load, P_m can be calculated using the following
 244 equations:

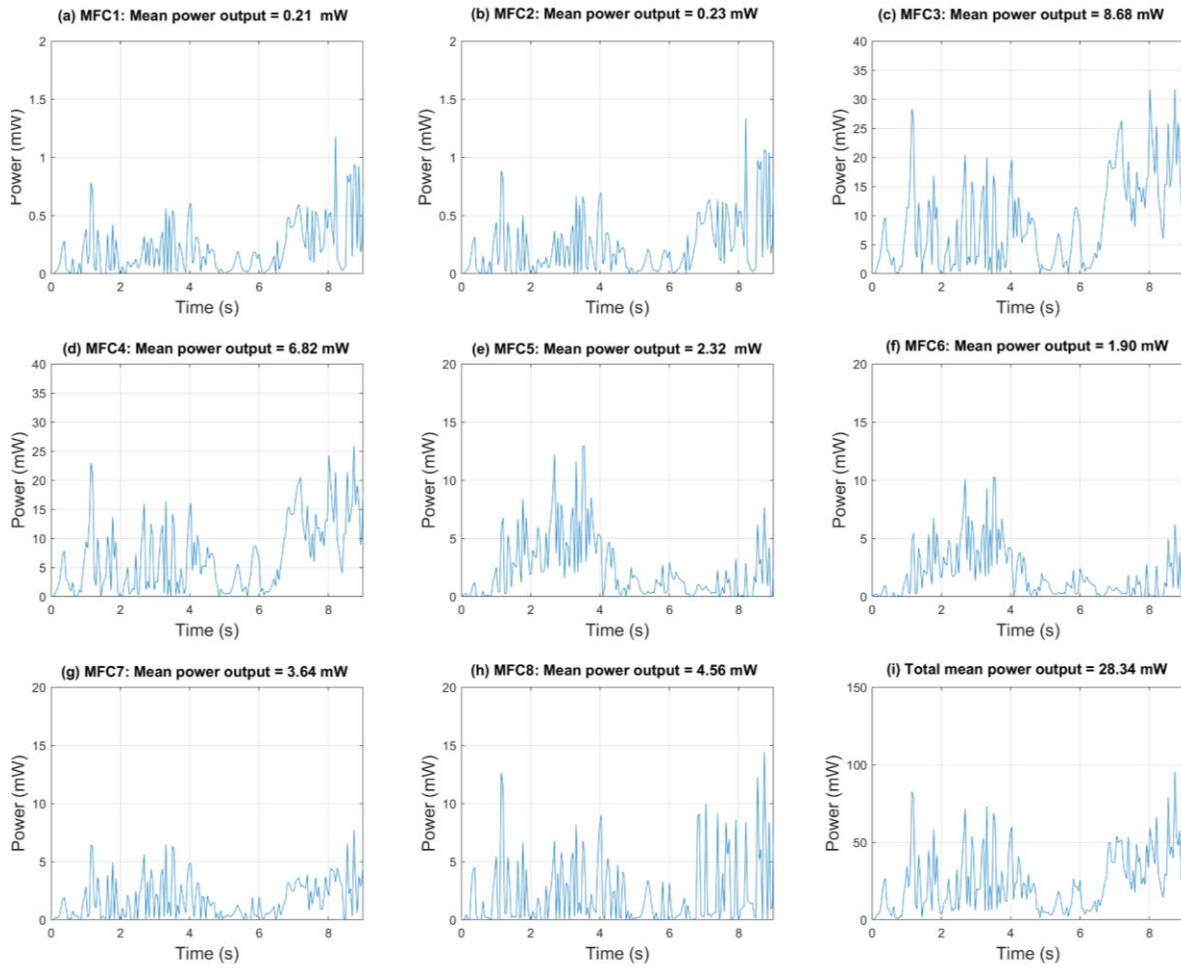
$$I_{load}(t) = \frac{I_{sc}^2(t) Z_i}{\sqrt{Z_i^2 + Z_{load}^2}} \quad (3)$$

$$Z_{load}(t) = Z_i(t) = \frac{1}{\omega(t) C_p} \quad (4)$$

$$P_m(t) = I_{load}^2(t) Z_{load} \quad (5)$$

245 where C_p is the capacitance of the piezoelectric material.

246 With the above-mentioned equations (1)-(5), the power output from each MFC piezoelectric
 247 material as well as the total power output were calculated and plotted in Figure 9. The total mean
 248 power output from 8 MFCs is 28.34 mW and the peak harvested power during the analysed time
 249 period exceeding 100 mW. However, this calculated power is unstable AC power, which is not
 250 suitable to transmit, store and distribute efficiently. For the purpose of a better conversion and
 251 management of the harvested energy, conditioned DC power are always adopted.



252
253

Figure 9. Power output calculated from 8 MFC piezoelectric materials.

254 *3.2. Rectified power prediction*

255 Since the harvested power is to be used to power electronic devices, which typically require DC
256 power supplies, rectification circuits are needed to provide usable DC power for potential loads. This
257 section provides the rectified output power estimation and analysis using both passive and popular
258 active rectification circuits. Full-bridge rectifiers (FBR) are widely used due to simplicity and stability;
259 however, the poor output power of FBRs hindered the development of active rectification circuits in
260 the past decade [33]. The synchronised switch harvesting (SSH) architecture is one of the most
261 promising rectification systems to provide high energy efficiency for piezoelectric energy harvesting
262 [34]. In this section, the output power from a passive FBR, switch-only (SO) and SSH on capacitors
263 (SSHC) was simulated and analysed to show the peak DC output of the proposed energy harvesting
264 system.

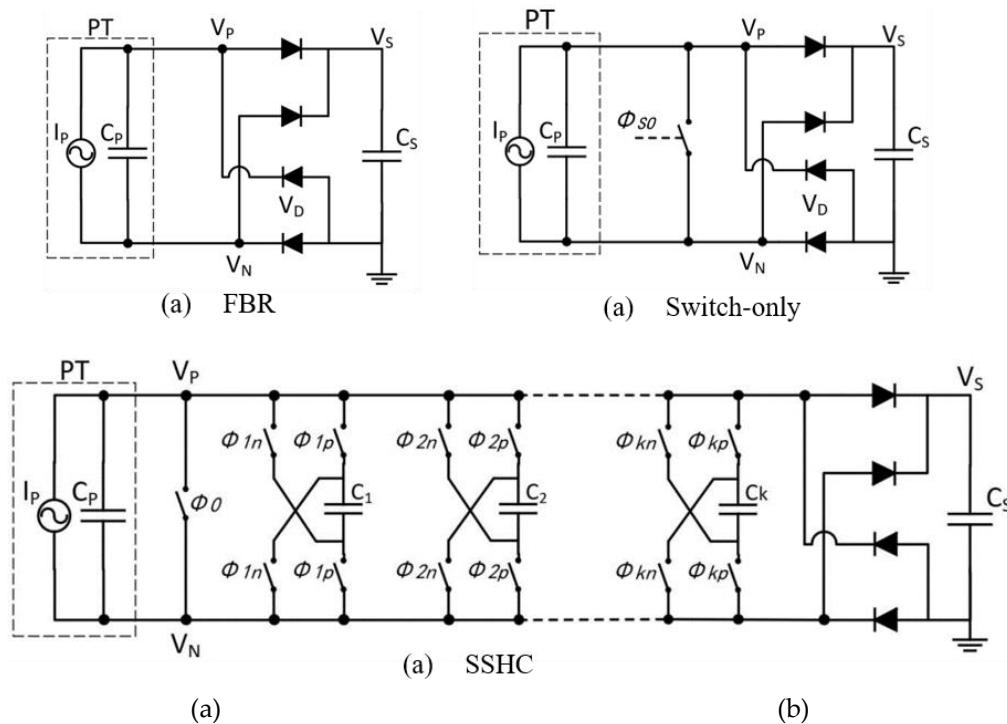


Figure 10. (a) Circuit diagram of an FBR, (b) a SO rectifier and (c) an SSHC rectifier.

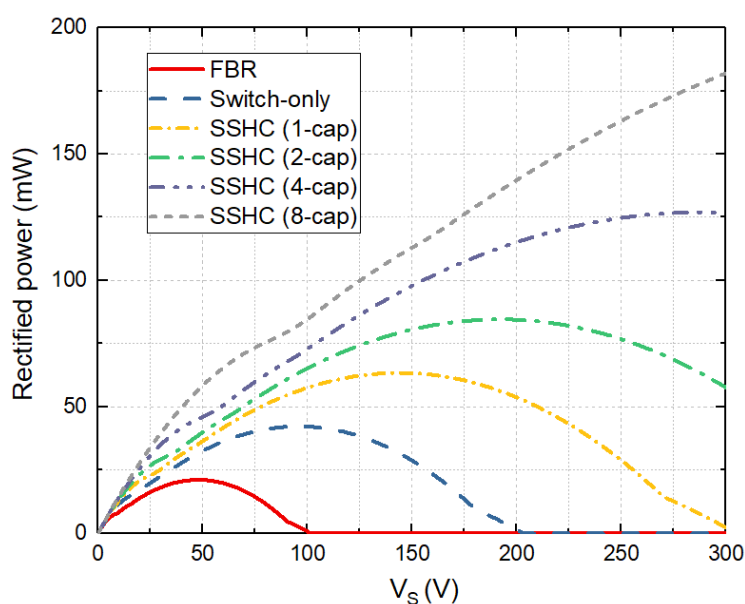
265

266 The circuit diagrams of an FBR, a SO rectifier and an SSHC rectifier are shown in Figure 8. In the
 267 diagrams, the piezoelectric transducer (PT) has been modelled as a current source (I_P) in parallel with
 268 its inherent capacitor (C_P). In these three rectifiers, only the FBR is a passive rectifier using 4 passive
 269 diodes. The SO and SSHC rectifiers are active rectifiers requiring additional circuit designs to
 270 generate the control signals to drive the switches. The circuit implementations of the SSHC rectifier
 271 have been detailed in [34]. The number k represents the number of capacitor stages to perform as a
 272 k -stage SSHC rectifier. The SO rectifier is a simplified SSHC rectifier with the ϕ_0 switch only by
 273 removing all the following capacitor stages. Hence, the SO rectifier can be also regarded as a zero-
 274 stage SSHC rectifier.

275 The rectified output power of all the eight MFC elements when using different rectification
 276 circuits was simulated and is shown in Figure 11. The simulations were based on the current sources
 277 calculated from the linear piezoelectric theory with the average stress outputs obtained from finite
 278 element analysis. The horizontal axis is the output voltage of the rectifier, which is also the voltage
 279 across the output capacitor connected at each rectification circuit, V_S , as shown in Figure 10. For the
 280 SSHC rectifier, different numbers of employed capacitors are simulated for various output power
 281 values with different performance levels. The more capacitors that are employed, the higher the peak
 282 output power that is achieved. However, more capacitors in SSHC rectifiers also result in more
 283 complicated control circuits, larger system sizes and higher optimal output voltage levels to achieve
 284 the peak power. The simulations were performed for V_S values ranging up to 300 V. The peak output
 285 power of each rectifier and the corresponding optimal output power are summarised in Table 5. From
 286 this table, it can be found that when using a passive FBR, the peak rectified power is around 21.2 mW
 287 from all the 8 MFC elements. When an 8-stage SSHC rectifier is employed, the peak rectified power
 288 achieves 181.9 mW, which is more than 8 times higher compared to a passive FBR. In order to
 289 achieve this high output power, the output voltage, V_S , of the SSHC rectifier needs to be maintained
 290 at around 300 V. Since this optimal voltage is usually higher than supply voltages for most low-power

291 loads, an efficiency DC-DC converter and a voltage regulator are typically required to power the load
292 electronics.

293 It is worthwhile analysing the power contributions from different MFC elements for future
294 design optimisations. The peak rectified output power values from individual MFC elements are
295 shown in Table 6. It can be clearly seen that the MFC 3 and MFC 4 contribute more than 90% of the
296 total rectified power. This is because MFC 3 and MFC 4 are mechanically located at stress
297 concentration regions (welding connections within the adjacent host structures), inducing a high
298 stress output and therefore the highest power output.



299

300 **Figure 11.** Simulated rectified output power using FBR, switch-only (SO) rectifier and SSHC rectifier
301 (with different numbers of capacitor stages) for all the eight MFC elements.

302 **Table 5.** Peak rectifier power for each rectification circuit and the corresponding optimal output voltage.

Rectifiers	Peak power (mW)	Optimal VS (V)
FBR	21.2	48
Switch-only	42.3	96
SSHC (1-cap)	63.4	144
SSHC (2-cap)	84.6	192
SSHC (4-cap)	126.9	288
SSHC (8-cap)	181.9	300

303

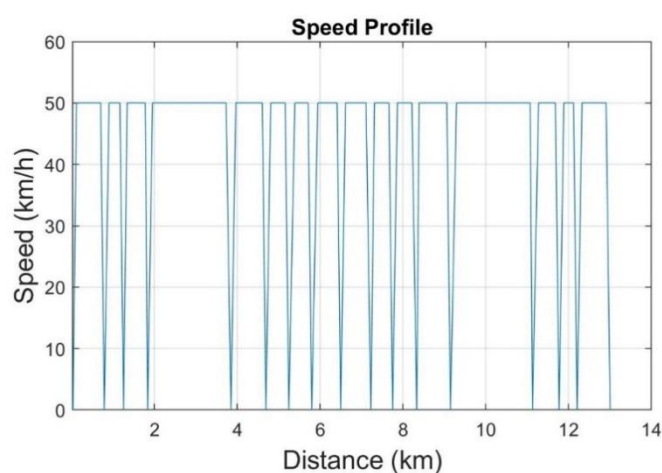
Table 6. Peak output power from individual MFC elements and their contributions to the total power.

MFC No.	Peak rectified power (mW)						Percentage (%)
	FBR	Switch-only	SSHC (1-cap)	SSHC (2-cap)	SSHC (4-cap)	SSHC (8-cap)	
1	0.28	0.56	0.84	1.12	1.68	2.79	1.2
2	0.31	0.61	0.92	1.23	1.84	3.06	1.3
3	11.89	23.78	35.67	47.57	71.35	118.92	51.7

4	9.34	18.68	28.01	37.35	56.03	93.38	40.6
5	0.24	0.47	0.71	0.94	1.41	2.36	1.0
6	0.19	0.39	0.58	0.77	1.16	1.94	0.8
7	0.35	0.69	1.04	1.38	2.07	3.46	1.5
8	0.41	0.82	1.22	1.63	2.45	4.08	1.8

304 4. Discussion on use of power budget

305 It is clear that the energy harvesting from the vehicle vibration itself is impossible to meet the
 306 power requirement of the motors and actuators, as the motive power requirement is more than an
 307 order of magnitude higher than what energy harvesting can provide. However, the recoverable
 308 power is sufficient to meet the power requirements of sensors, microprocessors and wireless systems
 309 which are important to railway infrastructures to regulate maintenance and to ensure safety. In order
 310 to study the impact of the recovered power a possible route for the new rail vehicle was analysed.
 311 The vehicle speed based on initial route assumptions is shown in Figure 12. The route is defined over
 312 a route of 14 km within the City of Coventry, with known locations of seventeen stop stations. The
 313 route speed limit is defined according to the standards in the United Kingdom. The entire running
 314 time period of one route is approximately 20 mins (1200 s) based on the speed limits.



315

316

Figure 12. Speed profile of this vehicle vs. distance.

317 In order to assess the meaningfulness of the calculated recoverable power, the typical power
 318 requirements of various functionally sensors, controller and wireless systems are summarised in
 319 Table 7. Some of the power consumptions do not need to be in active operation all the time and smart
 320 power management can help to reduce the power budget. A power requirement for one journey was
 321 estimated to be 153 mW and this could be met by the harvested power from the vehicle vibrations.
 322 Table 8 compares different types of rail harvesting sources from the open literature to evaluate the
 323 accuracy of the calculated power budget as well as to understand the harvested power contributions
 324 from a wide range of sources. Most of the literature investigated energy harvesting from train
 325 induced railway track vibrations, such as, Wang et al. [35] and Wang et al. [36] who proposed the use
 326 of an electromagnetic generator and piezoelectric transducers embedded in the track to harvest
 327 energy from the moving vehicle loads mainly via experimental testing. Cleante et al. [37] analytically
 328 investigated the amount of harvested energy induced by a passing train at various speeds using a
 329 trackside energy harvester. Tehrani et al. [38] analytically calculated a single spring-mass-damper
 330 system used as the energy harvester with the measured acceleration from a train cabin. Although
 331 these works contain basic analytical modelling, they lack consideration of sprung mass vibrations
 332 and the electronic network between various energy harvesters. Wheelwright et al. [39] established a

333 vibration-based condition system product for the monitoring, management and maintenance of
 334 wheelsets of rolling stock to prevent failures. In terms of the railway station network, Jiang et al. [40]
 335 built electronics storage schemes for regenerative energy from railway stations to reduce the
 336 operating costs and improve the operational safety of railways. However for the first time, this work
 337 takes account of energy harvesting from sprung mass vibrations in the train chassis using both finite
 338 element modelling of prototype design and electronics simulation optimisation, which is more
 339 representative of the realistic scenarios.

340 **Table 7.** Estimated power budget of the sensor platform with the application of the route assumption of this
 341 vehicle.

Power budget item	Power (mW)	Active in period (%)	Active time in one route cycle (s)	Power in one route cycle (mW)
MEMS 9 DOF motion sensor + MPU [41] ×2 units	0.05	100%	1200	1
Inclinometers [42] ×2 units	56.25	100%	1200	112.50
Distance sensors [43] ×2 units	13.95	100%	1200	27.90
Microprocessor unit (MPU) (active mode [44]) ×2 units	0.36	100%	1200	0.72
Bluetooth 5 + RF chip (transceiver mode [45]) ×2 units	27	20%	240	10.80
Bluetooth 5 + RF chip (sleep mode, clock [45]) ×2 units	0.045	80%	960	0.08
Sum				153.00

342 **Table 8.** Different types of energy harvested in the rail from the literatures.
 343

Type of rail harvesting	Energy harvest	Methodology	Comments
Train induced track vibration	2-4 volts	Experiments	For 6.35mm track displacement input, from Wang et al. [35]
	0.02 mW - 0.2 mW	Experiments Analytical modelling	For slack-type and patch-type piezoelectric transducers, from Wang et al. [36]
	100.3 mW - 157.1 mW	Analytical modelling	With passing train speed from 190 to 200 km/h, from Cleante et al. [37]
Electrification of railway stations	541.6 kW	Electronics simulation	Jiang et al. [40]
Unsprung mass vibration	21.4 mW	Analytical modelling	Ghandchi Tehrani et al. [38]
	1-5 wheel health index	Experiments	Wheelwright et al. [39]
Sprung mass vibration	21.2 mW - 181.9 mW	Finite element modelling Electronics simulation	This work

344 5. Conclusions

345 This paper presented the energy generation from a multifunctional MFC-embedded composite
 346 chassis of a rail structure. The rectification circuits are designed to help the optimisation and power
 347 management for harvested energy under the real-world vibration data measured in a cabin of a rail
 348 vehicle. A finite element model was built to numerically predict the time dependent stress responses

349 using representative three axis acceleration data. Eight locations were therefore determined at the
350 bottom chassis for integrating the piezoelectric energy harvesters. The analytical model was
351 developed to explain the energy harvesting mechanisms. The rectification circuit design of the
352 various passive and active rectification systems were proposed to design to help the optimisation and
353 management of harvested energy. The results showed that a peak of 181.9 mW DC electric power
354 was approximately recovered when an eight-stage SSHC rectifier was employed. Compared to the
355 other designs and case without such circuit design optimisation, its generates high output power
356 compared to the AC power, FBR and the switch-only rectifier which makes it suitable to meet the
357 required power budget. The power level achieved by harvesting operational vibration was
358 considered to be sufficiently and continuously sustain a simple sensor service platform, considering
359 a hypothetical average power budget consumption of 153 mW. The novel optimisation using
360 rectification circuits for improving the efficiency of energy harvesting has rarely been reported and
361 the success of maximising the energy harvested in this paper offers a significant opportunity to enable
362 micro-watt power scavenging from ambient vibrations towards the realistic applications.

363 In the near future, a prototype of the composite chassis of rail vehicle will be fabricated with
364 integration of energy harvesters based on the current design and optimised rectification circuits.
365 Experimental testing under mechanical vibrations with the various operational and environmental
366 conditions will be performed to validate this work which will point a route for further exploitation
367 not only in the rail industry, but also the automotive, offshore wind energy and aerospace sectors.
368

369 **Author Contributions:** Conceptualization, Y.L., S.D., Y.J. and Y.S.; Data curation, Y.L., S.D. and Y.J.;
370 Methodology, Y.L., S.D., Y.J. and Y.S.; Software, Y.L. and S.D.; Validation, Y.J., Y.S., and D.H.; Writing—review
371 and editing, Y.L., S.D., M.S., Y.J. and Y.S and D.H.; Visualization, M.S., Y.J., Y.S., and D.H.; Supervision, Y.J., Y.S.,
372 and D.H. All authors have read and agreed to the published version of the manuscript.

373 **Funding:** This research received no external funding.

374 **Acknowledgments:** This work was supported under the Coventry Light Rail Project at WMG, University of
375 Warwick, supported by Coventry City Council and the West Midlands Combined Authority. The vehicle
376 structure was designed in collaboration with TDI Ltd, UK.

377 **Conflicts of Interest:** The authors declare no conflict of interest.

378 Abbreviations

379 The following abbreviations are used in this manuscript:

380	CFRP	carbon fibre reinforced polymer
381	FBR	full-bridge rectifiers
382	FEA	finite element analysis
383	MFC	micro fibre composites
384	SO	switch-only
385	SSHC	synchronized switch harvesting capacitors

386 References

- 387 1. Zuo, L.; Tang, X. Large-scale vibration energy harvesting. *J. Intell. Mater. Syst. Struct.* 2013, 24, 1405–1430.
- 388 2. Zuo, L.; Scully, B.; Shestani, J.; Zhou, Y. Design and characterization of an electromagnetic energy harvester
389 for vehicle suspensions. *Smart Mater. Struct.* 2010, 19.
- 390 3. Glynne-Jones, P.; Tudor, M.J.; Beeby, S.P.; White, N.M. An electromagnetic, vibration-powered generator
391 for intelligent sensor systems. In *Proceedings of the Sensors and Actuators, A: Physical*; 2004; Vol. 110, pp.
392 344–349.
- 393 4. Erturk, A.; Inman, D.J. *Piezoelectric energy harvesting*; Wiley, 2011; ISBN 1119991358.
- 394 5. Lu, Q.; Liu, L.; Scarpa, F.; Leng, J.; Liu, Y. A novel composite multi-layer piezoelectric energy harvester.
395 *Compos. Struct.* 2018, 201, 121–130.
- 396 6. Jia, Y.; Yan, J.; Soga, K.; Seshia, A.A. Parametrically excited MEMS vibration energy harvesters with design
397 approaches to overcome the initiation threshold amplitude. *J. Micromechanics Microengineering* 2013, 23,
398 1–15.
- 399 7. Zhu, G.; Chen, J.; Liu, Y.; Bai, P.; Zhou, Y.S.; Jing, Q.; Pan, C.; Wang, Z.L. Linear-Grating Triboelectric

- 400 Generator Based on Sliding Electrification. *Nano Lett.* 2013, 13, 2282–2289.
- 401 8. Zhu, G.; Lin, Z.-H.; Jing, Q.; Bai, P.; Pan, C.; Yang, Y.; Zhou, Y.; Wang, Z.L. Toward Large-Scale Energy
- 402 Harvesting by a Nanoparticle-Enhanced Triboelectric Nanogenerator. *Nano Lett.* 2013, 13, 847–853.
- 403 9. Lafont, T.; Gimeno, L.; Delamare, J.; Lebedev, G.A.; Zakharov, D.I.; Viala, B.; Cugat, O.; Galopin, N.;
- 404 Garbuio, L.; Geoffroy, O. Magnetostrictive–piezoelectric composite structures for energy harvesting. *J.*
- 405 *Micromechanics Microengineering* 2012, 22, 094009.
- 406 10. Minsili, L.S.; Xia, H.; Eko, R.M. Analytical model of underground train induced vibrations on nearby
- 407 building structures in Cameroon: Assessment and prediction. *Leonardo Electron. J. Pract. Technol.* 2013,
- 408 12, 63–82.
- 409 11. Gill, K.S. Cognitive radio connectivity for railwa transportation networkds, 2017.
- 410 12. Tao, K.; Lye, S.W.; Miao, J.M.; Hu, X. Performance enhancement of an out-of-plane electret-based
- 411 vibrational energy harvester with dual charged plates. *J. Phys. Conf. Ser.* 2014, 557.
- 412 13. Li, H.; Tian, C.; Deng, Z.D. Energy harvesting from low frequency applications using piezoelectric
- 413 materials. *Appl. Phys. Rev.* 2014, 1.
- 414 14. Dai, H.L.; Abdelkefi, A.; Javed, U.; Wang, L. Modeling and performance of electromagnetic energy
- 415 harvesting from galloping oscillations. *Smart Mater. Struct.* 2015, 24, 45012.
- 416 15. Gao, M.; Wang, P.; Cao, Y.; Chen, R.; Cai, D. Design and Verification of a Rail-Borne Energy Harvester for
- 417 Powering Wireless Sensor Networks in the Railway Industry. *IEEE Trans. Intell. Transp. Syst.* 2017, 18,
- 418 1596–1609.
- 419 16. Alsaadi, A.; Shi, Y.; Pan, L.; Tao, J.; Jia, Y. Vibration energy harvesting of multifunctional carbon fibre
- 420 composite laminate structures. *Compos. Sci. Technol.* 2019, 178, 1–10.
- 421 17. Beeby, S.P.; Tudor, M.J.; White, N.M. Energy harvesting vibration sources for microsystems applications.
- 422 *Meas. Sci. Technol.* 2006, 17.
- 423 18. Sosnicki, O.; Lhermet, N.; Claeysen, F. Vibration energy harvesting in aircraft using piezoelectric
- 424 actuators. *Proc Actuator* 2006, 21, 968–971.
- 425 19. Shi, Y.; Hallett, S.R.; Zhu, M. Energy harvesting behaviour for aircraft composites structures using macro-
- 426 fibre composite: Part I – Integration and experiment. *Compos. Struct.* 2017, 160, 1279–1286.
- 427 20. Tianchen, Y.; Jian, Y.; Ruigang, S.; Xiaowei, L. Vibration energy harvesting system for railroad safety based
- 428 on running vehicles. *Smart Mater. Struct.* 2014, 23.
- 429 21. Pourghodrat, A.; Nelson, C.A.; Hansen, S.E.; Kamarajugadda, V.; Platt, S.R. Power harvesting systems
- 430 design for railroad safety. *Proc. Inst. Mech. Eng. Part F J. Rail Rapid Transit* 2014, 228, 504–521.
- 431 22. Hadas, Z.; Smilek, J.; Rubes, O. Energy harvesting from passing train as source of energy for autonomous
- 432 trackside objects. *MATEC Web Conf.* 2018, 211.
- 433 23. Du, S.; Jia, Y.; Arroyo, E.; Fernandez, S.; Riches, S.T.; Seshia, A.A. MEMS Piezoelectric Energy Harvester
- 434 Powered Wireless Sensor Module Driven by Noisy Base Excitation. In *Proceedings of the 2019 20th*
- 435 *International Conference on Solid-State Sensors, Actuators and Microsystems & Eurosensors XXXIII*
- 436 *(TRANSDUCERS & EUROSENSORS XXXIII)*, Berlin, Germany; 2019; pp. 350–353.
- 437 24. Jia, Y.; Yan, J.; Du, S.; Feng, T.; Fidler, P.; Middleton, C.; Soga, K.; Seshia, A.A. Real world assessment of an
- 438 auto-parametric electromagnetic vibration energy harvester. *J. Intell. Mater. Syst. Struct.* 2018, 29, 1481–
- 439 1499.
- 440 25. Du, S.; Jia, Y.; Zhao, C.; Chen, S.T.; Seshia, A.A. Real-world evaluation of a self-startup SSHI rectifier for
- 441 piezoelectric vibration energy harvesting. *Sensors Actuators, A Phys.* 2017, 264, 180–187.
- 442 26. Erturk, A.; Inman, D.J. An experimentally validated bimorph cantilever model for piezoelectric energy
- 443 harvesting from base excitations. *Smart Mater. Struct.* 2009, 18, 025009.
- 444 27. Erturk, A.; Inman, D.J. A Distributed Parameter Electromechanical Model for Cantilevered Piezoelectric
- 445 Energy Harvesters. *J. Vib. Acoust.* 2008, 130.
- 446 28. Jia, Y.; Wei, X.; Xu, L.; Wang, C.; Lian, P.; Xue, S.; Al-Saadi, A.; Shi, Y. Multiphysics vibration FE model of
- 447 piezoelectric macro fibre composite on carbon fibre composite structures. *Compos. Part B Eng.* 2019, 161,
- 448 376–385.
- 449 29. Winnett, J.; Hoffrichter, A.; Iraklis, A.; McGordon, A.; Hughes, D.J.; Ridler, T.; Mallinson, N. Development
- 450 of a very light rail vehicle. *Proc. Inst. Civ. Eng. - Transp.* 2016, 170, 231–242.
- 451 30. Gulf Coast Data Concepts X16-1D USB MEMS accelerometer data loggers; 2016;
- 452 Prepreg Fabric - GURIT SE84LV/RC200T/42% Available online:
- 453 https://www.900gpa.com/en/product/prepregCompound/FabPreg_00FABBBA10?u=metric (accessed on

- 454 Oct 16, 2019).
- 455 32. Microfibre composites (MFC) P2, P3 Type Available online: [https://www.smart-material.com/MFC-](https://www.smart-material.com/MFC-product-P2.html)
- 456 [product-P2.html](https://www.smart-material.com/MFC-product-P2.html) (accessed on Oct 15, 2019).
- 457 33. Du, S.; Jia, Y.; Zhao, C.; Amaratunga, G.A.J.; Seshia, A.A. A passive design scheme to increase the rectified
- 458 power of piezoelectric energy harvesters. *IEEE Trans. Ind. Electron.* 2018, 65, 7095–7105.
- 459 34. Du, S.; Jia, Y.; Zhao, C.; Amaratunga, G.A.J.; Seshia, A.A. A fully integrated split-electrode SSHC rectifier
- 460 for piezoelectric energy harvesting. *IEEE J. Solid-State Circuits* 2019, 54, 1733–1743.
- 461 35. Wang, J.J.; Penamalli, G.P.; Zuo, L. Electromagnetic energy harvesting from train induced railway track
- 462 vibrations. *Proc. 2012 8th IEEE/ASME Int. Conf. Mechatron. Embed. Syst. Appl. MESA 2012* 2012, 11787,
- 463 29–34.
- 464 36. Wang, J.; Shi, Z.; Xiang, H.; Song, G. Modeling on energy harvesting from a railway system using
- 465 piezoelectric transducers. *Smart Mater. Struct.* 2015, 24.
- 466 37. Cleante, V.G.; Brennan, M.J.; Gatti, G.; Thompson, D.J. Energy harvesting from the vibrations of a passing
- 467 train: Effect of speed variability. *J. Phys. Conf. Ser.* 2016, 744.
- 468 38. Tehrani, M.G.; Gatti, G.; Brennan, M.J.; Thompson, D.J.; Oscillator, L. Energy harvesting from train
- 469 vibrations. *11th Int. Conf. Vib. Probl.* 2013, 9–12.
- 470 39. Wheelwright, H.E.; Vincent, D. *Perpetuum*. 2019, pp. 1–16.
- 471 40. Jiang, B.Y.; Liu, J.; Tian, W.; Shahidehpour, M.; Krishnamurthy, M. Energy harvesting for the electrification
- 472 of railway stations. 2014, 39–48.
- 473 41. TDK-InvenSense Available online: [https://www.invensense.com/products/motion-tracking/9-axis/mpu-](https://www.invensense.com/products/motion-tracking/9-axis/mpu-9250/)
- 474 [9250/](https://www.invensense.com/products/motion-tracking/9-axis/mpu-9250/) (accessed on Oct 25, 2019).
- 475 42. SCA100T Inclinometers | Inclinometers | Sensors | Murata Manufacturing Co., Ltd. Available online:
- 476 <https://www.murata.com/en-sg/products/sensor/inclinometer/sca100t> (accessed on Oct 23, 2019).
- 477 43. SRF08 Ultrasonic Sensor Available online: <https://www.active-robots.com/srf08-ultrasonic-sensor.html>
- 478 (accessed on Oct 23, 2019).
- 479 44. STM32L4 - ARM Cortex-M4 ultra-low-power MCUs - STMicroelectronics Available online:
- 480 <https://www.st.com/en/microcontrollers-microprocessors/stm32l4-series.html> (accessed on Oct 23, 2019).
- 481 45. Darroudi, S.M.; Caldera-Sánchez, R.; Gomez, C. Bluetooth mesh energy consumption: A model. *Sensors*
- 482 (Switzerland) 2019, 19.
- 483



© 2020 by the authors. Submitted for possible open access publication under the terms and conditions of the Creative Commons Attribution (CC BY) license (<http://creativecommons.org/licenses/by/4.0/>).